

LOCAL STATISTICS FOR GENERATIVE IMAGE DETECTION

Yung Jer WONG and Teck Khim NG

School of Computing

National University of Singapore (NUS), Singapore

Abstract—Diffusion models (DMs) are generative models that learn to synthesize images from Gaussian noise. DMs can be trained to do a variety of tasks such as image generation and image super-resolution. Researchers have made significant improvement in the capability of synthesizing photorealistic images in the past few years. These successes also hasten the need to address the potential misuse of synthesized images. In this paper, we highlight the effectiveness of computing local statistics, as opposed to global statistics, in distinguishing digital camera images from DM-generated images. We hypothesized that local statistics should be used to address the spatial non-stationarity problem in images. We show that our approach produced promising results and it is also robust to various perturbations such as image resizing and JPEG compression.

I. INTRODUCTION

The idea of denoising diffusion was initially proposed by Sohl-Dickstein et al. in 2015 [1], drawing inspiration from non-equilibrium thermodynamics. Its development showed significant improvement when researchers overcame the difficulty of estimating gradients of the data distribution in latent space [2], [3], [4]. Since then, numerous research papers contributed significantly in the progress of generating high-quality images [4], [5], [6], [7], [8]. The work by Dhariwal and Nichol [9] demonstrated that diffusion models have emerged as the new state-of-the-art generative models, replacing generative adversarial networks (GANs) designed by Goodfellow et al. [10]. DMs offer the flexibility to precisely control the image generation process by conditioning on text prompts [11], [6], [7], [12]. In addition to image generation, DMs are also used for other tasks such as image super-resolution [13], [14], and medical image analysis [15], [16], [17].

Diffusion models transform random noise to a semantically meaningful image sample through iterative denoising. The assumption here is that the initial image sample only contains random noise sampled from Gaussian distribution. In each denoising step, an additive Gaussian noise is estimated by U-net [18] and removed from the image sample. This sequential denoising process ultimately produces a refined image that matches

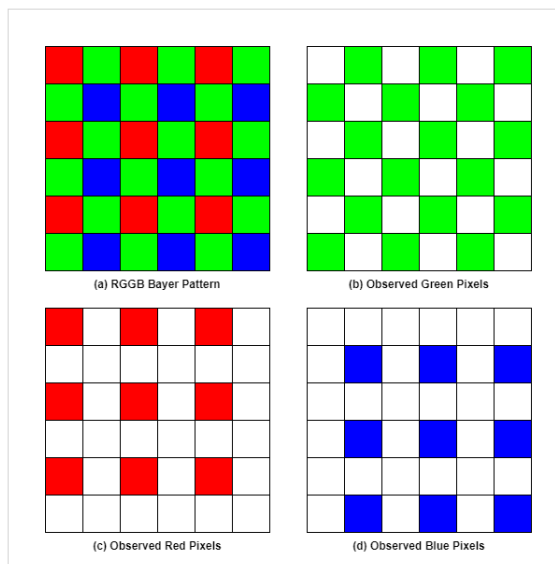


Figure 1: The RGGB Bayer pattern in color filters. Green pixels are sampled twice as many as the red pixels or the blue pixels. Other possible Bayer patterns include BGGR, GBRG and GRBG.

the training data distribution. However, real image noises can be more complex than the common assumption of Additive White Gaussian Noise (AWGN). Szeliski showed in [19] that real image noises are mostly introduced in the image sensing pipeline. These noises may include fixed pattern noise, dark current noise, shot noise, amplifier noise, and quantization noise. On the other hand, the noise of DM-generated images originates from the diffusion and denoising process. The difference in sources of noise therefore allows researchers to do image source attribution or distinguish fake images from real images [20], [21], [22].

In recent years, diffusion models, especially text-to-image diffusion models, have made synthetic image generation easy to consumers. As one of the most popular examples, Stable Diffusion [6] allows realistic and detailed images to be generated easily based on

users’ text prompts. In this paper, we specifically focus on the problem of detecting real images from synthesized images, using Stable Diffusion as a proxy for the synthesized images. We are inspired to develop methods for determining if an online image was generated by Stable Diffusion. Theoretically, there are two different ways of classifying real images from AI-generated images. Researchers can either identify concealed traces and patterns within generated images that are not found in real images; or identify traces and patterns within real images that are not present in generated images. We would use the later approach and address specifically the following problem: **“How to classify digital camera images from Stable Diffusion-generated images”**. We used *digital camera images* and *Stable Diffusion-generated images* to conduct all our experiments. We will present the performance of our proposed methods on both uncompressed images and images that are resized and compressed. This work aims to show the potential to exploit local image statistics to enable DM-generated image detection. Our work can be broken down into 2 parts as shown below.

- We verify that the hidden traces and patterns found in digital camera images are absent in Stable Diffusion images.
- We suggest three localized feature sets and prove why the combination of these feature sets can overcome JPEG compression and image resizing to successfully detect real digital camera images from Stable Diffusion generated (SD-generated) images.

II. RELATED WORK

This section briefly introduces the research work done in synthetic image detection and discusses how our approach is related to these methods.

Various methods leveraged handcrafted features such as texture analysis [23], [24], image inconsistencies [25], [26], [27], co-occurrence features [28] and artifact analysis [29]. In [30], [31] the authors substantiated the existence of artificial fingerprints in GAN-generated images. Subsequently, Zhang et al. [32] showed that adverse artifacts generally exist in the frequency domain of GAN-generated images. Frank et al. [33] explained that these artifacts are mainly caused by the upsampling operations that are currently utilized in all GAN architectures.

In recent years, many research papers were published and significant progress was seen in detecting DM-generated images. These works expanded from GAN-generated image detection and highlighted the limitations of certain methods that were effective on GAN-generated images but not on DM-generated images. Corvi et al. [34] showed that clear artifacts can be identified in the frequency domain of image residuals, extracted from

the original images using the denoising filter designed in [35]. Image residuals show distinctive and unique patterns in the frequency domain specific to their image source. By leveraging deep CNNs and the Residual Neural Networks (ResNets) designed by He et al. in [36], the authors of [34] managed to detect DM-generated images well. Wang et al. [37] utilized a pre-trained ADM [9] as a reconstruction model and DDIM [38] process to compute the Diffusion Reconstruction Error (DIRE). A pre-trained ResNet-50 [36] was then employed as the classifier. Most of the above mentioned methods involve the usage of deep neural networks to detect DM-generated images.

[34] also argued that data augmentation, especially image resizing, can negate many AI-generated image detection methods. Image resizing involves interpolation that may change or remove the high-frequency details in both authentic and synthetic images. Hence, to show the robustness of our proposed methods, we follow the image preprocessing procedures from the IEEE Video and Image Processing Cup 2022 [39], with slight modifications. Specifically, we apply random-cropping to the images using a ratio of $\frac{5}{8}$ and restrict the crop sizes to fall within the range [160, 2048], as suggested by Rahman et al. in the work [40]. Images are then resized to various dimensions before being compressed using the JPEG format with specific qualities.

We acknowledge the work by Gallagher and Chen, which involves detecting digital camera images through frequency analysis on diagonal variances in high-pass filtered images [41]. However, this early work does not effectively address the problem of spatial non-stationarity. The authors verified that most of the digital cameras employ camera sensors with Bayer filter, as shown in Figure 1. From this diagram, we observe that green pixels are sampled twice as many as the red or blue pixels in the Bayer mosaic. We notice a clear pattern: the diagonals are either filled solely with green pixels or alternating with red and blue pixels. In fact, this pattern is also found in the antidiagonals. The camera internal image processing pipeline will implement a demosaicing algorithm on the Bayer mosaic to reconstruct three separate full color channels. The values of the unobserved pixels in the three undersampled color channels are estimated with various interpolation methods such as bilinear and bicubic interpolation. This means that when the color channels of an image are reconstructed, all the unobserved pixels are estimated. The work in [42] revealed that linear interpolation leaves significant traces that can be easily detected because the estimated values for unobserved pixels are simply computed through a weighted linear combination of neighboring pixels. In particular, using the top-right illustration in Figure 1 as an example, Gallagher and Chen assumed that all

observed green pixels in the Bayer mosaic are I.I.D. with variance σ^2 [41]. The variance of the interpolated pixels, indicated as blank cells, will be smaller than σ^2 . Our derivation below shows that interpolated pixels have smaller variance than the observed pixels by assuming each unobserved pixel value is estimated by a *weighted linear combination of N neighboring pixels*:

$$\begin{aligned}
B(x_i, y_i) &= \sum_{(x_o, y_o) \in D} w_{(x_o, y_o)} B(x_o, y_o) \\
\sum_{(x_o, y_o) \in D} w_{(x_o, y_o)} &= 1 \\
\text{var}(B(x_o, y_o)) &= \sigma^2 \\
\text{var}(B(x_i, y_i)) &= \sum_{(x_o, y_o) \in D} w_{(x_o, y_o)}^2 \sigma^2 \\
0 &< w_{(x_o, y_o)} < 1 \\
0 &< w_{(x_o, y_o)}^2 < w_{(x_o, y_o)} < 1 \\
0 &< \sum_{(x_o, y_o) \in D} w_{(x_o, y_o)}^2 < \sum_{(x_o, y_o) \in D} w_{(x_o, y_o)} = 1 \\
\text{var}(B(x_i, y_i)) &< \text{var}(B(x_o, y_o))
\end{aligned}$$

where subscript i represents “interpolated” pixels’ coordinates; subscript o represents “observed” pixels’ coordinates; D is the set of all pixel coordinates that are used to estimate an unobserved pixel value; B represents the local Bayer mosaic similar to the top-right diagram in Figure 1.

Theoretically, it is possible to extract all the diagonals from the green channel of any input image and compute the variances of each diagonal to produce a “signal”. This signal will display an alternating pattern of high and low variances. Frequency analysis methods such as Discrete Fourier Transform (DFT) can help detect where the dominant frequency occurs. The peak is expected to occur at half the normalized frequency because diagonal variances alternate between high and low values. This is also true if we use anti-diagonals from the green channel. Since this demosaicing pattern is only observed in digital camera images, synthetic images do not exhibit a peak at the same frequency.

III. METHODOLOGY

We note that the diagonals that span across various image regions suffer from spatial non-stationarity. Complex regions tend to have higher variance in pixel values due to the presence of sharp edges or rapid changes in pixel intensity. Flat regions tend to have lower variance in pixel values. We address the spatial non-stationarity problem in our proposed method. Our method comprises three distinct feature sets. These three feature sets exploit localized image processing techniques to mitigate the problems caused by spatial non-stationarity. To ensure

the naming consistency, we will refer to them as *Features (1)*, *Features (2)* and *Features (3)*. We also provide detailed descriptions of these three approaches and explain why they are effective in generated image detection.

For Features (1), we first use a global high-pass filter to remove low frequency information. However, this does not sufficiently mitigate the spatial non-stationarity. We show that in addition to using a simple high-pass filter on the entire image, we should also use a local gradient operation to mitigate spatial non-stationarity in the image. We therefore propose to use a combination of a high-pass filter followed by a 2x2 filter that implements a localized gradient operation to generate Features (1). Computing the local rate of change of pixel intensity in high frequency details can effectively alleviate image non-stationarity. This is imperative to differentiate between DM-generated images and digital camera images. The 2x2 filters for diagonals and anti-diagonals are given respectively by the two kernels shown below:

$$\begin{bmatrix} 1 & 0 \\ 0 & -1 \end{bmatrix} \quad \begin{bmatrix} 0 & 1 \\ -1 & 0 \end{bmatrix}$$

We calculate the absolute gradients of both diagonals and anti-diagonals in the high-pass filtered green channel for Features (1). This helps reduce the influence of global variations due to image non-stationarity.

We exploited two more localized processing approaches to create Features (2) and Features (3).

For Features (2), we divide the image into non-overlapping blocks of 10x10 pixels. We compute the diagonal and anti-diagonal variances within each block. We then sum up all the variances of each block. The result is a *block-reduced* image of variances. The window size of 10x10 for the block reduction was determined empirically by conducting multiple experiments. Our last step for obtaining Features (2) is to sum up all the variances of the block-reduced image to obtain a single variance for each color channel. This is our Features (2).

We note that our Features (2) has some similarity with the work by Gallagher and Chen [41] in that we both compute the variances of pixels. Our approach differs however in three aspects: (a) We don’t need to perform a high pass filtering prior to variance computation; (b) We compute local statistics (i.e. variances of diagonals and anti-diagonals) instead of global statistics like in [41]; (c) We made use of all three color channels instead of just the green channel. We verified that our localized processing approach is more effective than [41].

Our Features (3) made use of the local variances computed for Features (2). We note that real digital camera images may exhibit variations in pixel distribution among the color channels due to the difference in the number of sampled pixels in each channel. This will not be the case for synthetic images because diffusion

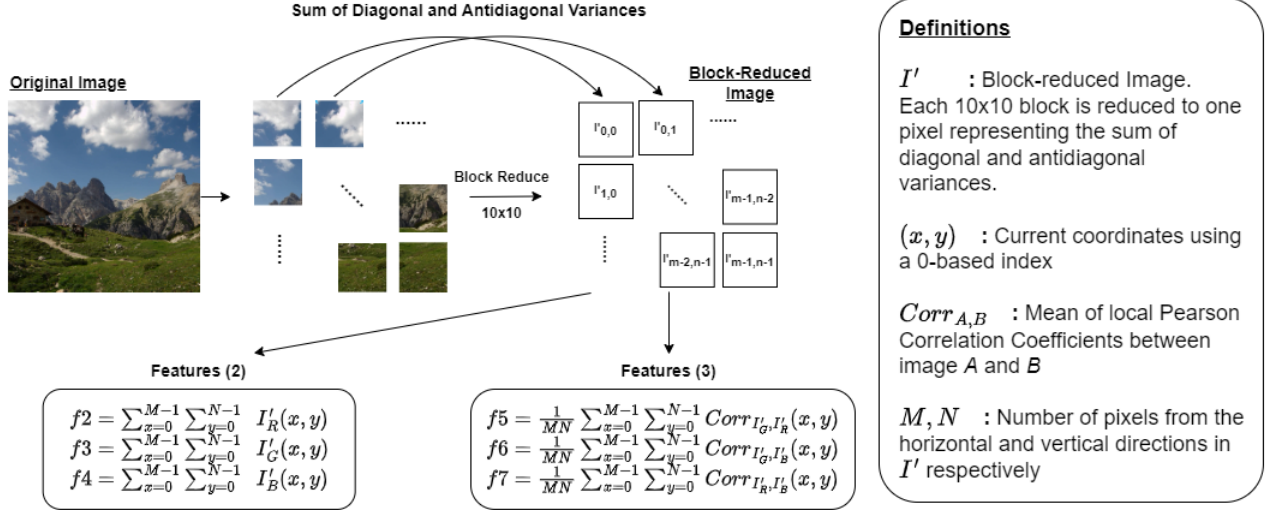


Figure 2: Flow diagram of the pipeline used for extracting Features (2) and Features (3). Each feature set comprises 3 individual features.

models assume white noise that follows a Gaussian distribution. Therefore, the differences in sum of local diagonal and anti-diagonal variances among all three color channels can be observed. We compute the local Pearson correlation of the block-reduced image variances established in Features (2). For authentic images, the local correlation is lower than generative images due to the difference in numbers between green pixels and red or blue pixels sampled by the camera sensors. However, for DM-generated images, the local correlation is higher because there is no demosaicing pattern that contributes to the difference in local correlations. All pixels in DM-generated images are the outputs of the backward diffusion process and image noise is assumed to follow a Gaussian distribution. We show that block-reduced matrices of color channels are highly correlated due to the common assumption of additive noise following a Gaussian distribution.

We will show in our experiments that our method is still effective even when image resizing and compression are done to the images. Despite the resampling of pixel values (resizing) and removal of high frequency details (compression), the underlying pixel distribution still retains the information about the pixel value changes in all three color channels.

In summary, we introduce a method consisting of three distinct feature sets. Each feature set utilizes localized processing operations to effectively detect DM-generated images, even when they have been resized and compressed. We showed in our experiments that our method achieved state-of-the-art performance in detecting real from diffusion generated images.

Figure 2 shows the steps for extracting Features (2)

and Features (3). In contrast to most of the recent works, our method is a non-deep learning approach. Deep neural networks are shown to be effective in detecting generated images in recent research. However, challenges in interpretability, computational cost and the need for a large number of high-quality labeled samples still remain unsolved. We will demonstrate the effectiveness of using our proposed features in the next section.

IV. EXPERIMENT SETUP

This section describes the dataset, train-test split, model parameters and the standardized procedures for image resizing used in all the following experiments.

We conduct detailed analyses on sample images obtained from 2 sources, i.e. *RAISE* dataset [43] and *DiffusionDB* dataset [44]. The composition of the dataset is shown in Table I.

Source	Subset	No. Images
RAISE [43]	RAISE_1k	1000
DiffusionDB [44]	large_random_1k	1000

Table I: Composition of dataset.

To show robustness and versatility, all experiment results of the method we proposed are based on models whose train size is only **10%** of the dataset. We chose XGBoost, a robust tree boosting classifier, as the standardized classifier and its model parameters are fixed as: $n_estimators:300$, $learning_rate:0.1$, $n_jobs:-1$, $eval_metric:"logloss"$, $objective:"multi:softmax"$, $num_class:2$. We also follow the same image preprocessing procedures as shared in the research work [40] to ensure the image resizing and

compression reflect the real world scenarios. These procedures are also in accordance with the IEEE VIP Cup 2022 standards [34]. However, slight modification is made to ensure that experimental results are comparable for different output sizes. Specifically, images are resized to various output sizes, not limited to 200x200, to evaluate both image resizing algorithms: *bicubic interpolation* and *area interpolation*. These images are further compressed using JPEG format with specified qualities.

V. RESULTS AND DISCUSSION

In this section, we first show the classification performance of our proposed method for varying random-crop output sizes and JPEG compression quality factors. The results are also compared with DIRE, one of the most recent generated-image detectors [37]. Then, we compare the approach leveraging diagonal variances proposed in [41] with our Features (1) that utilized diagonal gradients to mitigate spatial non-stationarity. We use image samples from *RAISE* [43] and *DiffusionDB* [44] datasets to represent digital camera images and DM-generated images respectively. The *DiffusionDB* dataset is retrieved via HuggingFace [45].

Four distinct experiments are conducted to study the classification performance of our proposed method. In the first experiment, our method is tested against varying random-crop output sizes. We apply random-cropping with pre-determined output sizes to the sample images. The output size, which struck a balance between a high Area Under the Curve (AUC) score and small image dimensions, will remain fixed for the three following experiments. For the three following experiments, we introduced a hypothetical scenario where input images may undergo preprocessing with a fixed probability to assess robustness. Therefore, the evaluation of the three following experiments will involve classifying both unprocessed and pre-processed images. We conduct the experiments in the following manners:

- 1) Each image has **70%** chance of undergoing JPEG compression (2^{nd} experiment), image resizing (3^{rd} experiment) or both (4^{th} experiment). The image resizing procedures follow the IEEE VIP Cup 2022 standards [34] and are referred from the work [40].
- 2) For images that are not resized, they will only be random-cropped to pre-determined dimensions.

While generating Features (2) and Features (3), we opted for a block size of 10x10 to break the 8x8 local block structures of JPEG compression. We did not explore what would be the optimal block size in our experiments. The AUC scores of our method, which combines Features (1)(2)(3), across varying random-crop output sizes and JPEG compression quality factors, are displayed in Table II. We also include the AUC scores

Size	Our Method		DIRE [37]	
	Original	Resized	Original	Resized
1024	0.995	0.835	0.316	0.316
512	0.960	0.777	0.337	0.329
256	0.975	0.821	0.252	0.294
128	0.918	0.802	0.337	0.330
64	0.902	0.771	0.493	0.426

Quality	Our Method		DIRE [37]	
	Compressed	R. & C.	Compressed	R. & C.
95	0.903	0.845	0.309	0.368
90	0.909	0.838	0.299	0.364
80	0.907	0.850	0.314	0.361
60	0.905	0.842	0.304	0.389
40	0.912	0.847	0.309	0.379
20	0.921	0.847	0.331	0.369

Table II: The comparison between our method and the DIRE detector [37] on our dataset. “R. & C.” is the abbreviation for “resized and compressed”. *Top*: The comparison of AUC scores between uncompressed and resized images across varying output sizes. *Bottom*: The comparison of AUC scores for images that are either only compressed or random-cropped followed by resizing and compression using various JPEG compression qualities. Image outputs are standardized to dimensions of 256x256. All the AUC scores are rounded to the nearest 3 s.f.

of the DIRE detector [37] on our dataset in the same table for comparison. We note that DIRE was trained on DiffusionForensics diffusion-generated image dataset whereas we trained our system on DiffusionDB SD-generated image dataset. We conducted a cross-dataset evaluation by testing DIRE as well as our method on both DiffusionDB and DiffusionForensics datasets. The results are shown in Table III. Note that our method performed significantly better than DIRE even though we only used 10% of the dataset for training.

The following experiment is conducted to compare the early method in [41] and our Features (1). The AUC comparison table is shown in Table IV. We notice improved AUC scores across all image dimensions when employing Features (1). At the point on the ROC curve with the fewest errors, 30 out of 1800 images (0.9833% acc.) were wrongly classified when employing the early method in [41]. On the contrary, only 13 out of 1800 images (0.9928% acc.) were wrongly classified when employing our Features (1).

Next, we investigate how varying compression quality factors can affect the classification results. This experiment is conducted at a fixed dimensions of 1024x1024, which had previously produced excellent results in the first experiment. Input images are initially random-cropped to a maximum size of 1024x1024 and sub-

	Our Method				DIRE [37]	
	ADM		IDDPM		DiffusionDB	
	Original	Resized	Original	Resized	Original	Resized
1024	-	0.813	-	0.804	0.682	0.648
512	-	0.684	-	0.677	0.685	0.644
256	0.977	0.760	0.978	0.752	0.626	0.629
128	0.942	0.698	0.942	0.677	0.548	0.615
64	0.914	0.667	0.921	0.659	0.531	0.576

Quality	Our Method				DIRE [37]	
	ADM		IDDPM		DiffusionDB	
	Compressed	R. & C.	Compressed	R. & C.	Compressed	R. & C.
95	0.941	0.632	0.943	0.630	0.510	0.471
90	0.933	0.663	0.938	0.647	0.499	0.470
80	0.934	0.591	0.935	0.590	0.501	0.473
60	0.926	0.614	0.923	0.595	0.515	0.474
40	0.924	0.651	0.930	0.650	0.507	0.482
20	0.926	0.649	0.923	0.646	0.502	0.476

Table III: The comprehensive cross-dataset evaluation between our method and the DIRE detector [37]. “R. & C.” is the abbreviation for “resized and compressed”. To ensure a fair comparison, we only interchanged the synthetic image representation in both datasets because they are diffusion-generated. Most of the images in the DIRE dataset do not reach the dimensions of 512x512, therefore we ignore the results for 512x512 and 1024x1024 for original, uncompressed images. ADM [9] and IDDPM [5] refer to the samples from their respective diffusion models sampled from the DiffusionForensics dataset [37]. All results are generated using 900 images per class following our experimental settings.

Crop Size	Features (1)	Diagonal Variances [41]
None	1.000	0.999
1024	0.994	0.991
512	0.858	0.826
256	0.941	0.887
128	0.790	0.713
64	0.739	0.719

Table IV: Comprehensive AUC comparisons of the method proposed in the early work [41] and our Features (1). All the values are rounded to the nearest 3 s.f. *None* indicates that no random-cropping is applied to the images. The results show that our Features (1) outperform the early work in all image dimensions.

Crop Size	Features (1)	Diagonal Variances [41]
95	0.606	0.601
90	0.619	0.588
80	0.636	0.604
60	0.633	0.595
40	0.627	0.591
20	0.626	0.607

Table V: The comparison of AUC scores between the method of [41] and our Features (1) for varying JPEG compression qualities. Input images are initially random-cropped to a maximum size of 1024x1024 and subsequently compressed at different quality factors.

sequently compressed at different quality factors. The distinct AUC scores across various compression qualities are shown in Table V. We observe that both the classifiers perform consistently poorly across all scenarios of different compression quality factors. Even Features (1),

Resized Dimensions	AUC of Features (2)(3)
1024	0.756
512	0.822
256	0.851
128	0.821
64	0.881

Table VI: Distinct AUC scores of Features (2)(3) for varying resized dimensions. All images are first resized to the specific dimensions, then compressed with a random JPEG compression quality $q \in [75, 95]$.

which outperforms the method by [41], performs poorly on compressed images. This is because standard compression methods such as JPEG compression erase subtle differences in images thereby making the classification task more challenging. Furthermore, it is worth noting that image resizing, as an image processing method, involves resampling all pixels that may further destroy the demosaicing pattern. Figure 3 compares the feature distributions of the method by [41] and our Features (1), along with Features (2) and Features (3), before and after image resizing and compression. We observed that Features (1) and the method proposed in [41] are less effective after image resizing and compression because the inter-cluster distance was reduced and cluster overlapping happened. Figure 3 illustrates the need to further exploit localized processing operations and employ Features (2) and Features (3) to address the problems of image resizing and compression. We demonstrate a detailed ablation study on the effect of Features (2) and

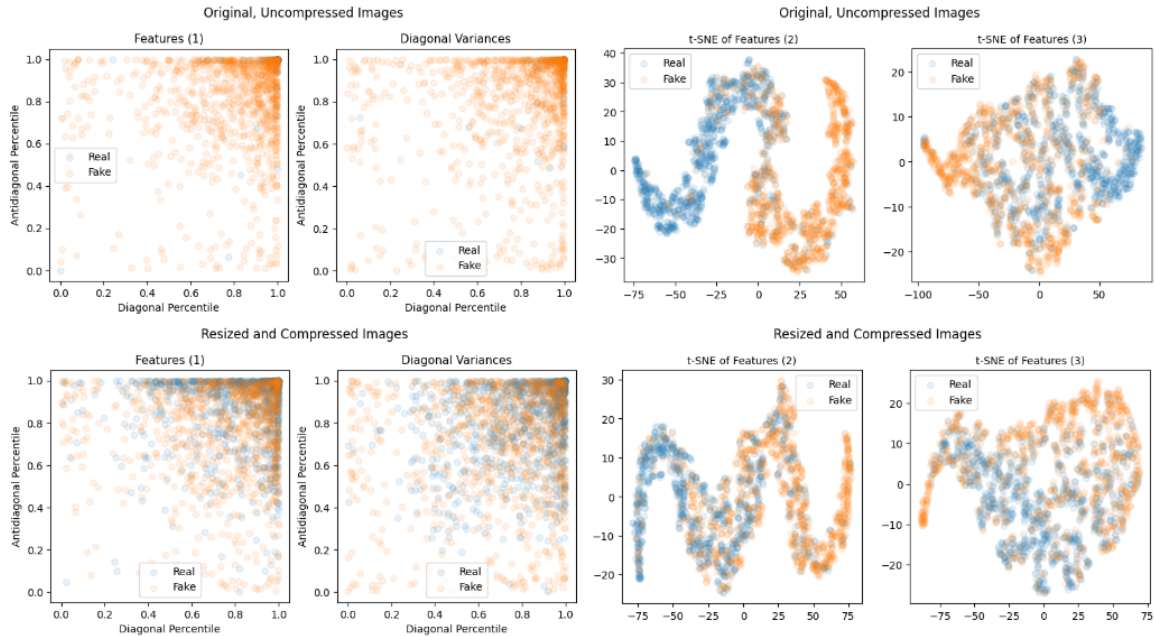


Figure 3: The plots illustrate the change in feature distribution when images are resized and compressed. *Top*: The feature distribution of original, uncompressed images compared across various approaches. *Bottom*: The feature distribution of resized and compressed images compared across various approaches. T-distributed neighbor embeddings (T-SNE) [46] visualized data points in high dimensions for Features (2)(3). The opacity of data points is set to 0.1. Blue data points represent camera images, and orange data points represent SD-generated images.

Features (3) in the following experiments.

Initially, we present the classification performance of Features (2)(3) on resized and compressed images. Table VI shows the classification performance of Features (2)(3) across varying resized dimensions. The images are further compressed with a random JPEG compression quality $q \in [75, 95]$. The results demonstrate the effectiveness of Features (2)(3) even after image resizing and compression. Subsequently, we provide the comparison between classifiers with and without Features (2)(3). We standardize the image dimensions for parity in result comparison. We decide to conduct the following experiment with images of dimensions **256x256** and the reasons are:

- Based on Table II, the image dimensions of 256x256 balance a high AUC score while ensuring fast computation results.
- Even though Stable Diffusion [6] generates images of dimensions 512x512 by default, many online DM-generated images are found to have sizes of 128x128 or 256x256 because generating smaller images requires lower memory usage and computational power.

Following the settings of the 4th experiment in which

images are potentially random-cropped, resized and compressed, we train 3 different classifiers: a classifier that used Features (1)(2)(3); a classifier that only used Features (1); and a classifier that only used Features (2)(3). The ROC curves across different compression qualities for the 3 classifiers and all their corresponding AUC scores are shown in Figure 4 and Table VII respectively. The results demonstrate that while Features (1) perform well on uncompressed, original images, Features (2) and (3) are necessary complements to classify images that are potentially resized and compressed.

The detailed experiments shown above suggest that a combination of the three feature sets, Features (1)(2)(3), is effective regardless of whether images are resized and compressed.

VI. CONCLUSION

In this paper, we described a method combining three localized processing approaches and their corresponding feature sets to detect generative images. Instead of finding traces concealed in DM-generated images, we chose to find unique traces that are present in digital camera images but not in DM-generated images. We first demonstrated the classification performance of our proposed method. Then, we compared the early method suggested in [41] with our Features (1) and showed

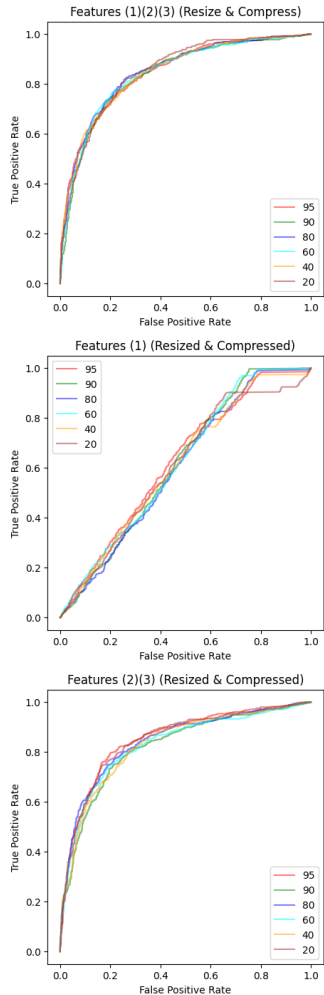


Figure 4: The plots above show the versatility of Features (2)(3) in classifying images that are potentially resized and compressed. *Top*: ROC curves of the classifier that uses Features (1)(2)(3), across different compression qualities. *Middle*: ROC curves of the classifier that uses only Features (1). *Bottom*: ROC curves of the classifier that uses Features (2)(3). We observe significant improvement in the classification performance after including Features (2)(3) when the train samples consist of both unprocessed and pre-processed images.

that Features (1) alone outperforms the early method. We also revealed that JPEG compression and image resizing actually made the early method [41] ineffective. Even though Features (1) also failed with JPEG compression and image resizing, they perform well as a system when combined with Features (2)(3) which leverage local statistics in block-reduced images and the local correlation between color channels respectively. All experiment results of our proposed method were obtained by training only on **randomly selected 10%**

JPEG Quality Factor	Features (1)(2)(3)	Features (1)	Features (2)(3)
95	0.861	0.625	0.845
90	0.854	0.617	0.856
80	0.878	0.603	0.868
60	0.848	0.621	0.862
40	0.861	0.612	0.840
20	0.847	0.606	0.863

Table VII: Comprehensive AUC comparisons to verify if it is necessary to include Features (2)(3) to complement Features (1). We observe that a classifier is bad when it utilized only Features (1). The AUC scores increased significantly for all JPEG compression quality factors after adding Features (2)(3). All the values are rounded to the nearest 3 s.f.

of samples per class. This shows the efficiency and robustness of our proposed method compared to state-of-the-art classifiers which requires much more samples to train.

REFERENCES

- [1] J. Sohl-Dickstein, E. Weiss, N. Maheswaranathan, and S. Ganguli, "Deep unsupervised learning using nonequilibrium thermodynamics," in *International Conference on Machine Learning*, pp. 2256–2265, PMLR, 2015.
- [2] Y. Song and S. Ermon, "Generative modeling by estimating gradients of the data distribution," *Advances in neural information processing systems*, vol. 32, 2019.
- [3] Y. Song, J. Sohl-Dickstein, D. P. Kingma, A. Kumar, S. Ermon, and B. Poole, "Score-based generative modeling through stochastic differential equations," *arXiv preprint arXiv:2011.13456*, 2020.
- [4] J. Ho, A. Jain, and P. Abbeel, "Denoising diffusion probabilistic models," *Advances in Neural Information Processing Systems*, vol. 33, pp. 6840–6851, 2020.
- [5] A. Q. Nichol and P. Dhariwal, "Improved denoising diffusion probabilistic models," in *International Conference on Machine Learning*, pp. 8162–8171, PMLR, 2021.
- [6] R. Rombach, A. Blattmann, D. Lorenz, P. Esser, and B. Ommer, "High-resolution image synthesis with latent diffusion models," in *Proceedings of the IEEE/CVF Conference on Computer Vision and Pattern Recognition*, pp. 10684–10695, 2022.
- [7] S. Gu, D. Chen, J. Bao, F. Wen, B. Zhang, D. Chen, L. Yuan, and B. Guo, "Vector quantized diffusion model for text-to-image synthesis," *arXiv preprint arXiv:2111.14822*, 2021.
- [8] D. Kingma, T. Salimans, B. Poole, and J. Ho, "Variational diffusion models," *Advances in neural information processing systems*, vol. 34, pp. 21696–21707, 2021.
- [9] P. Dhariwal and A. Nichol, "Diffusion models beat gans on image synthesis," *Advances in Neural Information Processing Systems*, vol. 34, pp. 8780–8794, 2021.
- [10] I. Goodfellow, J. Pouget-Abadie, M. Mirza, B. Xu, D. Warde-Farley, S. Ozair, A. Courville, and Y. Bengio, "Generative adversarial networks," *Communications of the ACM*, vol. 63, no. 11, pp. 139–144, 2020.
- [11] A. Nichol, P. Dhariwal, A. Ramesh, P. Shyam, P. Mishkin, B. McGrew, I. Sutskever, and M. Chen, "Glide: Towards photorealistic image generation and editing with text-guided diffusion models," *arXiv preprint arXiv:2112.10741*, 2021.
- [12] C. Saharia, W. Chan, S. Saxena, L. Li, J. Whang, E. L. Denton, K. Ghasemipour, R. Gontijo Lopes, B. Karagol Ayan, T. Salimans, et al., "Photorealistic text-to-image diffusion models with deep language understanding," *Advances in Neural Information Processing Systems*, vol. 35, pp. 36479–36494, 2022.
- [13] C. Saharia, J. Ho, W. Chan, T. Salimans, D. J. Fleet, and M. Norouzi, "Image super-resolution via iterative refinement," *IEEE Transactions on Pattern Analysis and Machine Intelligence*, 2022.
- [14] H. Li, Y. Yang, M. Chang, S. Chen, H. Feng, Z. Xu, Q. Li, and Y. Chen, "Srdiff: Single image super-resolution with diffusion probabilistic models," *Neurocomputing*, vol. 479, pp. 47–59, 2022.
- [15] A. Kazerouni, E. K. Aghdam, M. Heidari, R. Azad, M. Fayyaz, I. Hacihaliloglu, and D. Merhof, "Diffusion models for medical image analysis: A comprehensive survey," *arXiv preprint arXiv:2211.07804*, 2022.
- [16] M. Özbey, S. U. Dar, H. A. Bedel, O. Dalmaz, Ş. Öztürk, A. Güngör, and T. Çukur, "Unsupervised medical image translation with adversarial diffusion models," *arXiv preprint arXiv:2207.08208*, 2022.
- [17] J. Wolleb, F. Bieder, R. Sandkühler, and P. C. Cattin, "Diffusion models for medical anomaly detection," in *Medical Image Computing and Computer Assisted Intervention—MICCAI 2022: 25th International Conference, Singapore, September 18–22, 2022, Proceedings, Part VIII*, pp. 35–45, Springer, 2022.
- [18] O. Ronneberger, P. Fischer, and T. Brox, "U-net: Convolutional networks for biomedical image segmentation," in *Medical Image Computing and Computer-Assisted Intervention—MICCAI 2015: 18th International Conference, Munich, Germany, October 5–9, 2015, Proceedings, Part III 18*, pp. 234–241, Springer, 2015.
- [19] R. Szeliski, *Image Formation*, pp. 27–83. Cham: Springer International Publishing, 2022.
- [20] J. Lukas, J. Fridrich, and M. Goljan, "Digital camera identification from sensor pattern noise," *IEEE Transactions on Information Forensics and Security*, vol. 1, no. 2, pp. 205–214, 2006.
- [21] L. Verdoliva, "Media forensics and deepfakes: an overview," *IEEE Journal of Selected Topics in Signal Processing*, vol. 14, no. 5, pp. 910–932, 2020.
- [22] D. Cozzolino and L. Verdoliva, "Noiseprint: A cnn-based camera model fingerprint," *IEEE Transactions on Information Forensics and Security*, vol. 15, pp. 144–159, 2019.
- [23] B. Xu, J. Liu, J. Liang, W. Lu, and Y. Zhang, "Deepfake videos detection based on texture features," *Computers, Materials & Continua*, vol. 68, no. 1, 2021.
- [24] T. Fu, M. Xia, and G. Yang, "Detecting gan-generated face images via hybrid texture and sensor noise based features," *Multimedia Tools and Applications*, vol. 81, no. 18, pp. 26345–26359, 2022.
- [25] X. Yang, Y. Li, and S. Lyu, "Exposing deep fakes using inconsistent head poses," in *ICASSP 2019-2019 IEEE International Conference on Acoustics, Speech and Signal Processing (ICASSP)*, pp. 8261–8265, IEEE, 2019.
- [26] H. Farid, "Lighting (in) consistency of paint by text," *arXiv preprint arXiv:2207.13744*, 2022.
- [27] H. Farid, "Perspective (in) consistency of paint by text," *arXiv preprint arXiv:2206.14617*, 2022.
- [28] L. Nataraj, T. M. Mohammed, S. Chandrasekaran, A. Flenner, J. H. Bappy, A. K. Roy-Chowdhury, and B. Manjunath, "Detecting gan generated fake images using co-occurrence matrices," *arXiv preprint arXiv:1903.06836*, 2019.
- [29] Y. Li and S. Lyu, "Exposing deepfake videos by detecting face warping artifacts," *arXiv preprint arXiv:1811.00656*, 2018.
- [30] F. Marra, D. Gragnaniello, L. Verdoliva, and G. Poggi, "Do gans leave artificial fingerprints?," in *2019 IEEE conference on multimedia information processing and retrieval (MIPR)*, pp. 506–511, IEEE, 2019.
- [31] N. Yu, L. S. Davis, and M. Fritz, "Attributing fake images to gans: Learning and analyzing gan fingerprints," in *Proceedings of the IEEE/CVF international conference on computer vision*, pp. 7556–7566, 2019.
- [32] X. Zhang, S. Karaman, and S.-F. Chang, "Detecting and simulating artifacts in gan fake images," in *2019 IEEE international workshop on information forensics and security (WIFS)*, pp. 1–6, IEEE, 2019.
- [33] J. Frank, T. Eisenhofer, L. Schönherr, A. Fischer, D. Kolossa, and T. Holz, "Leveraging frequency analysis for deep fake image recognition," in *International conference on machine learning*, pp. 3247–3258, PMLR, 2020.
- [34] R. Corvi, D. Cozzolino, G. Zingarini, G. Poggi, K. Nagano, and L. Verdoliva, "On the detection of synthetic images generated by diffusion models," in *ICASSP 2023-2023 IEEE International Conference on Acoustics, Speech and Signal Processing (ICASSP)*, pp. 1–5, IEEE, 2023.
- [35] K. Zhang, W. Zuo, Y. Chen, D. Meng, and L. Zhang, "Beyond a gaussian denoiser: Residual learning of deep cnn for image denoising," *IEEE transactions on image processing*, vol. 26, no. 7, pp. 3142–3155, 2017.
- [36] K. He, X. Zhang, S. Ren, and J. Sun, "Deep residual learning for image recognition," in *Proceedings of the IEEE conference on computer vision and pattern recognition*, pp. 770–778, 2016.
- [37] Z. Wang, J. Bao, W. Zhou, W. Wang, H. Hu, H. Chen, and H. Li, "Dire for diffusion-generated image detection," in *Proceedings of the IEEE/CVF International Conference on Computer Vision (ICCV)*, pp. 22445–22455, October 2023.
- [38] J. Song, C. Meng, and S. Ermon, "Denoising diffusion implicit models," *arXiv preprint arXiv:2010.02502*, 2020.
- [39] L. Verdoliva, D. Cozzolino, F. Guillaro, R. Corvi, and K. Nagano, "Ieee video and image processing cup." <https://grip-unina.github.io/vipcup2022/>, 2022.
- [40] M. A. Rahman, B. Paul, N. H. Sarker, Z. I. A. Hakim, and S. A. Fattah, "Artifact: A large-scale dataset with artificial and factual

- images for generalizable and robust synthetic image detection,” *arXiv preprint arXiv:2302.11970*, 2023.
- [41] A. C. Gallagher and T. Chen, “Image authentication by detecting traces of demosaicing,” in *2008 IEEE Computer Society Conference on Computer Vision and Pattern Recognition Workshops*, pp. 1–8, IEEE, 2008.
- [42] A. C. Gallagher, “Detection of linear and cubic interpolation in jpeg compressed images,” in *The 2nd Canadian Conference on Computer and Robot Vision (CRV’05)*, pp. 65–72, IEEE, 2005.
- [43] D.-T. Dang-Nguyen, C. Pasquini, V. Conotter, and G. Boato, “Raise: A raw images dataset for digital image forensics,” in *Proceedings of the 6th ACM multimedia systems conference*, pp. 219–224, 2015.
- [44] Z. J. Wang, E. Montoya, D. Munechika, H. Yang, B. Hoover, and D. H. Chau, “DiffusionDB: A large-scale prompt gallery dataset for text-to-image generative models,” *arXiv:2210.14896 [cs]*, 2022.
- [45] Q. Lhoest, A. V. del Moral, Y. Jernite, A. Thakur, P. von Platen, S. Patil, J. Chaumond, M. Drame, J. Plu, L. Tunstall, *et al.*, “Datasets: A community library for natural language processing,” *arXiv preprint arXiv:2109.02846*, 2021.
- [46] L. Van der Maaten and G. Hinton, “Visualizing data using t-sne.,” *Journal of machine learning research*, vol. 9, no. 11, 2008.